J. Fluid Mech. (1997), *vol.* 337, *pp.* 49–66

The velocity field near moving contact lines

By Q. CHEN, E. RAMÉ AND S. GAROFF†

Department of Physics *and* Colloids, Polymers, and Surfaces Program,
Carnegie Mellon University, Pittsburgh, PA 15213, USA

(Received 17 April 1996 and in revised form 21 October 1996)

The dynamics of a spreading liquid body are dictated by the interface shape and flow field very near the moving contact line. The interface shape and flow field have been described by asymptotic models in the limit of small capillary number, *Ca*. Previous work established the validity and limitations of these models of the interface shape (Chen *et al*. 1995). Here, we study the flow field near the moving contact line. Using videomicroscopy, particle image velocimetry, and digital image analysis, we simultaneously make quantitative measurements of both the interface shape and flow field from 30 μm to a few hundred microns from the contact line. We compare our data to the modulated-wedge solution for the velocity field near a moving contact line (Cox 1986). The measured flow fields demonstrate quantitative agreement with predictions for $Ca \leqslant 0.1$, but deviations of $\sim 5\%$ of the spreading velocity at $Ca \approx 0.4$. We observe that the interface shapes and flow fields become geometry independent near the contact line. Our experimental technique provides a way of measuring the interface shape and velocity field to be used as boundary conditions for numerical calculations of the macroscopic spreading dynamics.

1. Introduction

Dynamic wetting, the displacement of one fluid by another immiscible fluid over a solid surface, controls many natural and technological phenomena, such as coating deposition and oil recovery. Spreading has been studied extensively both experimentally and theoretically (Dussan 1979; de Gennes 1985; Kistler 1993). When surface tension forces are important, the interface shape and the local flow field very near the moving contact line control the macroscopic configuration of the fluid body. However, identifying the correct modelling assumptions needed for predictive models of spreading is not trivial in the theoretical development or in experimental investigation. Theoretically, the central difficulty is the unphysical stress singularity at the contact line that arises when the classical hydrodynamic assumptions (Newtonian and incompressible fluids, non-deformable solids, and the continuity of the velocities at the boundaries) are applied up to and including the moving contact line (Huh & Scriven 1971; Dussan & Davis 1974). The singularity suggests that very near the moving contact line, unique microphysical processes other than classical hydrodynamics control the fluid motion. While theorists have suggested models for these unique microphysical processes (Dussan 1976; Huh & Mason 1977; Hocking 1977; Voinov 1994; de Gennes, Hua & Levinson 1990; Tuck & Schwartz 1990; Yang, Koplik & Banavar 1992; Thompson & Robbins 1990), none of these ideas have been experimentally confirmed. Experimentally, direct observation of fluid motion in the region where the unique hydrodynamics operate (assumed to be less than 10 μm from

† To whom correspondence should be addressed.

the contact line) is not accessible by conventional accurate optical techniques. Ngan & Dussan (1979) showed that, in contrast to static wetting, the measurement of an apparent dynamic contact angle near the contact line strongly depends on the macroscopic scale. Therefore, such measurements made in one geometry may not be used to predict the dynamics in a different geometry.

While the identity of the microphysical processes near the contact line is not yet established, models predicting the macroscopic spreading process have been reported (Hocking & Rivers 1982; Cox 1986; Dussan, Ramé & Garoff 1991). Based on matched asymptotic expansions, these models assume that information about the unique hydrodynamics is transferred from an inner region very near the moving contact line (where the unique microphysical processes operate), through an intermediate region (where surface tension and viscous forces dominate), to an outer region (where the macroscopic geometry dominates). In these models, the detailed nature of the inner-region hydrodynamics need not be specified, only its asymptotic behaviour must be established. The asymptotic solution of Dussan *et al.* (1991) describes the dynamic interface shape in the intermediate and the beginning of the outer regions, at zero Reynolds number, in the limit of capillary number $Ca \to 0$. Chen, Ramé & Garoff (1995) established the validity and limitations of the predictions for the interface shape. For poly(dimenthylsiloxane) (PDMS) spreading on the clean surface of a Pyrex tube, this model describes the interface shape at $20 \leqslant r \leqslant 400$ μm up to $Ca = 0.1$, where r is the distance from the contact line. Systematic breakdown has been found for higher Ca.

In this paper, we describe our study of the flow field near the moving contact line. We compare our experimental measurements to the model of Cox (1986) which assumes that the flow field near the moving contact line is controlled by the local geometry of the wedge-like region formed between the solid surface and the liquid/air interface. This local flow field is, therefore, independent of the macroscopic geometry of the spreading fluid body. The velocity gradients of the flow field generate the viscous forces which bend the interface beyond the curvature caused by the static pressure jump across the interface. In the polar coordinate system illustrated in figure 1, the velocity field is

$$\tilde{v}_r = \frac{v_r(r,\phi,\beta)}{U} = \frac{\beta\cos\phi + \phi\sin\beta\sin(\phi-\beta) - \sin\beta\cos(\phi-\beta)}{\Delta}, \tag{1}$$

$$\begin{aligned}\tilde{v}_\phi &= \frac{v_\phi(r,\phi,\beta)}{U} \\ &= \frac{-\beta\sin\phi + \phi\sin\beta\cos(\phi-\beta)}{\Delta} \\ &\quad + r\left(\frac{\mathrm{d}\beta}{\mathrm{d}r}\right)\left(\frac{2\sin^2\beta(\beta\sin\phi - \phi\sin\beta\cos(\phi-\beta))}{\Delta^2} - \frac{\sin\phi - \phi\cos(2\beta-\phi)}{\Delta}\right),\end{aligned} \tag{2}$$

where $\Delta \equiv \beta - \sin\beta\cos\beta$, U is the velocity of the contact line relative to the solid surface, (r,ϕ) is a polar coordinate system with the origin at the contact line and the solid at $\phi = 0$, and $\phi = \beta(r)$ is the location of the interface. In (1) and (2) the shape of the interface influences the velocities. The capillary number enters indirectly through the interface shape. All the velocities in the rest of this paper are scaled with the spreading velocity, unless the units are specified after the value of the velocity.

The flow described by (1) and (2), called 'modulated-wedge' flow in the rest of this

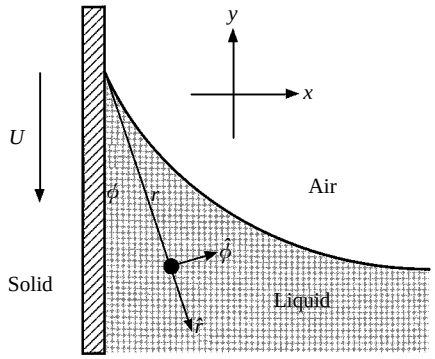

FIGURE 1. Coordinate system.

paper, is based on zero-Reynolds-number flow in a fixed-angle wedge derived by Moffatt (1964) and Huh & Scriven (1971). While compatible with the model for the interface shape discussed above, this modulated-wedge flow field model is much more general. In the modulated wedge, the boundaries can be liquid/air or solid/liquid interfaces. The only restrictions are that: (i) the region described by the model must be much smaller than any other length scale of the system; (ii) the shape of the interface must be a slowly changing function of r. The physical bases of these two assumptions for the modulated wedge solution are the following.

(i) Dussan & Davis (1974) showed that all flows of incompressible fluids undergoing two-dimensional Stokes flow and obeying the no-slip condition at the solid/liquid interface have the following structure near a moving contact line:

$$v(r,\phi) = v_w(\phi) + v_R(r,\phi), \tag{3}$$

where $v_w(\phi) \equiv \lim_{r\to 0} v(r,\phi)$. Equation (3) is a definition for $v_R(r,\phi)$. Because v_w does not depend on r, it is not affected by any geometrical length scale of the system: v_w is the flow in a fixed-angle wedge. The velocity field v_R is a residual component having the following properties: (*a*) from the definition of $v_w(\phi)$, v_R has a well-defined limit as $r\to 0$, i.e. $v_R(0,\phi) = 0$; and (*b*) because v_R is affected by the geometrical length scales of the system, $v_R(r,\phi)$ represents the macroscopic contribution to the flow near the contact line.

Thus, $v_w(\phi)$ is the limit of all Stokes flows near moving contact lines; and the macroscopic contribution, $v_R(r,\phi)$, must decay to zero as $r\to 0$. The rate at which $v_R(r,\phi)\to 0$ as $r\to 0$ is controlled by the smallest length scale of the problem where departures from the limiting wedge geometry occur (e.g. tube radius, container dimensions).

(ii) This argument extends to the case of the modulated-wedge flow, where the extra assumption that the square of the dimensionless interface curvature $(\mathrm{d}\beta/\mathrm{d}\ln r)^2 \ll 1$ must hold. The modulated-wedge solution is a perturbation of the fixed-angle wedge solution valid when $(\mathrm{d}\beta/\mathrm{d}\ln r)^2 \ll 1$. In this approximation, the flow at any distance $r = r^*$ is equal to the fixed-angle wedge flow that would develop if the fixed wedge angle were $\beta(r^*)$. $\phi = \beta(r)$ is the shape of the boundary satisfying $(\mathrm{d}\beta/\mathrm{d}\ln r)^2 \ll 1$, hence the term 'modulated wedge'. Any portion of the interface where $(\mathrm{d}\beta/\mathrm{d}\ln r)^2$ is not small represents a departure from the geometry required for the modulated-wedge theory to describe the flow. Thus, the distance from the contact line where this departure occurs introduces a new macroscopic length scale. In order for the flow to be described by this theory, we must move toward the contact line away from the region where $(\mathrm{d}\beta/\mathrm{d}\ln r)^2$

is not small so that $v_R(r, \phi)$ makes a negligible contribution to the total flow v. Thus, the effect of violating $(\mathrm{d}\beta/\mathrm{d}\ln r)^2 \ll 1$ at one location spreads beyond this location, causing a non-local breakdown of the modulated wedge approximation.

We explore the fundamental hydrodynamic phenomena in the region within the first few hundred microns from the moving contact line, which bridges from the microscopic to the macroscopic scales of the fluid body spreading on solid surfaces. In this work, we measure the flow fields near the contact line and compare the data to the modulated-wedge model. For the first time, simultaneous measurements of the interface shape and the velocity field are performed near the moving contact line. By direct comparison between the data and the model, we test the validity of the model. We also investigate the geometry-free portions of the interface shape and flow field data. These geometry-free data provide boundary conditions for predictive calculations of spreading.

In the next section, we describe our experimental set-up and data acquisition. We emphasize the error analyses which are crucial to the conclusions we draw later. Our results are presented in §3. We first show some general features of the flow field near the moving contact line and then compare the data to the modulated-wedge solution. Finally, we analyse the geometry-independent flow fields as well as the interface shapes. We summarize our conclusions in §4.

2. Experimental

We make simultaneous measurements of the liquid/air interface shape and liquid velocity field near the moving contact line. Measurements are achieved by immersing a clean Pyrex cylindrical tube into a bath of PDMS at constant speed. The PDMS wets the Pyrex completely forming a static contact angle of zero. At the capillary numbers probed in the experiments discussed in this paper, we have determined that precursing films are not present on the Pyrex surface ahead of the moving contact line. We employ videomicroscopy, particle image velocimetry (PIV) and digital image analysis.

2.1. *Experimental set-up and data acquisition*

The apparatus set-up and material preparation are the same as those used in earlier studies of dynamic wetting (Marsh 1992; Marsh, Garoff & Dussan 1993; Chen *et al.* 1995; Ramé & Garoff 1996). During the experiment, the dynamic liquid/air interfaces are formed by driving a clean Pyrex tube (outer diameter ~ 1.25 cm) into a bath of PDMS (60 000 cSt at 25 °C) contained in a square glass optical cell (10 cm a side) at constant speeds (35–150 μm s^{-1}). All the measurements reported here are performed with the contact line below the bulk fluid level so that both the interface shape and velocity field can be measured at the same time. Small bubbles and dust particles with diameter from 3 to 15 μm in the PDMS are the visible tracers used to measure the liquid velocity fields by PIV (Mertzkirch 1974). We back light the meniscus with uniform lighting provided by Koehler illumination (Inoue 1986). A long-working-distance microscope connected to a CCD camera captures the images of meniscus profiles and seed particles in the liquid. The digitized images are then stored in the computer for further analysis. See figure 2 for a typical image.

The data analysis involves finding the shape of the interface and the position of the particles as a function of time. We first use the frame grabber of the computer to capture a sequence of frames separated by equal time intervals. The time interval Δt is varied depending on the immersion speed of the tube so that the distance between two consecutive data points is roughly the same at all speeds. For $Ca = 0.10$, Δt is

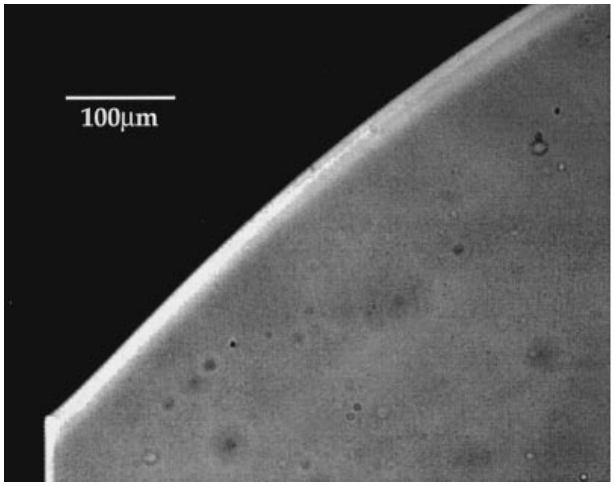

FIGURE 2. Typical image with enhanced contrast. Interface in capillary depression. Dark regions are solid surface and air. Bright region is liquid. Some small seed particles can be seen inside the liquid.

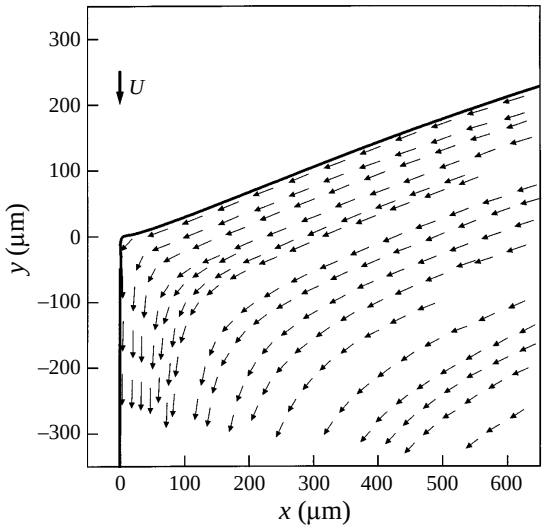

FIGURE 3. A typical flow field near the moving contact line at $Ca = 0.1$. The solid line represents the solid surface and the liquid/air interface. The bold arrow marks tube immersion velocity, $U = 35$ μm s^{-1}. Only every fifth data point is shown.

about 0.60 s; for $Ca = 0.43$, Δt is about 0.10 s. Steady-state conditions are ensured by checking that the interface shape stays the same over the sequence of frames. The digitized image consists a 640×480 array of grey levels. The interface location is obtained as the set of points with the highest grey level gradient in the same manner as in previous studies (Marsh *et al.* 1993; Chen *et al.* 1995). Particle images are typically 3–10 pixels across. The particle positions are determined by identifying the centre of the particle image by eye. The velocity is the local first derivative of position with respect to time.

Figure 3 is an example of the measured vector velocity field. Full two-dimensional plots of the difference between two vector velocity fields are hard to interpret. Thus, we plot the magnitude and direction of the vector field differences as a function of r only,

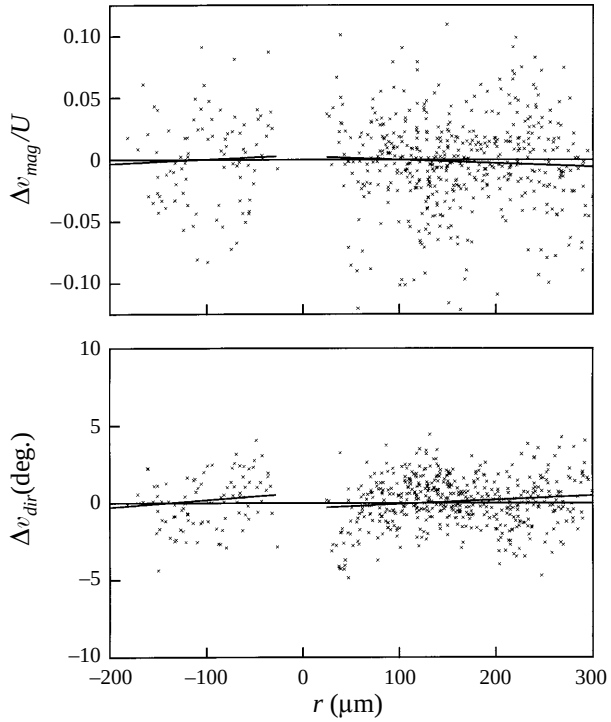

FIGURE 4. Typical reproducibility. Data at $Ca = 0.43$. v_{dir} = direction of velocity, v_{mag} = magnitude of velocity. The lines are second-order polynomial fits to the difference of data sets.

without regard to the polar variable. When important information is contained in the polar variations, we note them. We define the distance of the particle from the contact line, r, as positive as a particle approaches the contact line and negative as it moves away. Evidently, data points with positive r come from roughly the upper half of the fluid wedge, and with negative r from the lower half of the fluid wedge. This produces plots such as figure 4. There will be smooth solid lines on all the figures showing the data. These are obtained by best fitting the data with a second- or third-degree polynomial. These lines are fit to data points at $r > 0$ and $r < 0$ separately. They represent the average of data in the upper and lower halves of the wedge space and clarify the trends in the data clouds.

The uncertainties and the reproducibility of the data are crucial to the conclusions we draw. In the rest of this section, we discuss and evaluate the random and systematic uncertainties. The error analyses of the interface shape data are the same as we described in Chen *et al.* (1995). For the velocity data, we first discuss the uncertainties in the measured velocity. This allows us to evaluate the significance of differences between velocity data sets. Then, we analyse the uncertainty in the theoretical velocity which arises from the experimental input needed to calculate the theory. This allows us to evaluate the deviation of the experimental data from the predictions of the modulated-wedge model.

2.2. *Uncertainties in experimental data*

The random errors in velocity data arise from the particle position determination and the uncertainties in time intervals between each frame. Typically, the uncertainty of a position datum is ± 0.5 pixel (~ 0.6 μm in most of our runs) in both the x- and y-

directions. We estimate the time interval uncertainty to be half the time of a video frame, ± 0.017 s. The particle trajectories cannot contain spatial variations with wavelengths on the order of the spacing of the data points, typically ~ 20 μm. Thus, we can safely smooth the random scatter of the data by fitting each data point and four of its neighbouring points (two on each side) to a second-degree polynomial (Savitzky & Golay 1964). The differences between smoothed and original data randomly scatter around zero, showing that no systematic distortion is introduced by the smoothing process. The velocities are then calculated by taking the first derivative of the smoothed position data with respect to time. The smoothing process greatly reduces the uncertainties in velocities to ± 0.01 in the scaled magnitude and $\pm 1.5°$ in the direction.

There are four sources of systematic uncertainty in the velocity measurements: (i) convective flow of the PDMS due to room temperature gradients; (ii) inertial effects causing the particles to fail to follow fluid point trajectories, especially as the particle turns sharply near the moving contact line; (iii) particles moving in a plane that is not exactly parallel to the focal plane; (iv) uncertainty in the contact line position. We estimate the size of each of these systematic errors and determine the uncertainties they cause in the measured velocity.

(i) We observe a macroscopic flow across the glass container even when the tube is not moving. Its magnitude is less than 1 μm s^{-1} and gets much smaller near the solid tube surface. The general flow forms loops on the scale of the container, and may move either clockwise or counterclockwise. Since the Péclet number, $Pe \sim 10^6$, the observed particle motion is not particle diffusion. Analyses of the temperature gradients across our cell ($\leqslant 0.01$ °C), the density-driven and Marangoni-driven flows for our problem, indicate that this fluid motion is convection due to density gradients in the PDMS. While 1 μm s^{-1} is a typical convective velocity, it decreases by a factor of ~ 30 within 1000 μm from the tube surface. The convection in the region near the tube surface (where our measurements concentrate) will then be less than 0.001 of the tube velocity and therefore may be ignored compared to other uncertainties in the experiment.

(ii) To accurately map the fluid flow fields, our particles must follow fluid elements in the time interval of each velocity measurement. The inertia of the particles does not cause a significant deviation of the particle from the fluid point trajectory over the time of one velocity measurement (five adjacent position data). The Reynolds number based on the size and the density of the particle is $\sim 10^{-8}$. Thus, particles will follow fluid point trajectories through curved streamlines, at least for the time of the measurement. We can further justify neglecting inertial effects by considering the worst case in our experiment: the motion of particles near the moving contact line where the velocity gradient is the greatest. As the particle turns near the corner, the viscous force balances the centripetal force. Assuming the particle is spherical, this balance implies

$$m\frac{v_{particle}^2}{L} \sim 6\pi R\mu\,|v_{particle} - v_{fluid}|, \tag{4}$$

where L is the radius of curvature of the fluid trajectory, R is the radius of the particle and m the mass of the particle. For typical values in our experiment ($R \sim 10$ μm, $v \sim 100$ μm s^{-1}, $L \sim 10$ μm near the contact line), (4) implies that the particle velocity should vary from the fluid velocity by 10^{-7} μm s^{-1} in the direction towards the contact line. This is beyond the detectability limit of our experiments.

(iii) Because of the depth of field of the microscope, we observe particles within $\sim \pm 200$ μm of the focal plane. If a particle moved outside the focal plane but within the depth of field, the particle image would remain relatively sharp. Typically, in our experiments, a particle image does not change noticeably as the particle moves across

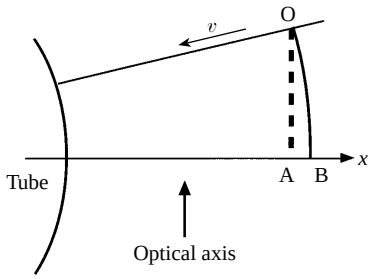

FIGURE 5. Effect of particle outside of the focal plane. O: Actual particle position. A: Apparent position. B: Position producing correct theoretical velocity.

the field of view (~ 800 μm). Thus, the velocity component normal to the focal plane can be no more than 1.5% of the component parallel to the focal plane. Therefore, although the flow field is three-dimensional due to our experimental geometry, the velocity component normal to the focal plane is not significant.

Because the microscope only shows the particle image projected on the plane parallel to the focal plane, the observed distance travelled by particles is the projection of the real distance on the focal plane (see figure 5). This projection makes the velocity magnitude appear smaller. Given the tube radius of 1.25 cm and the field of view of 800 μm, the measured velocity is lower than the real velocity by $< 0.01\%$. This is also beyond our detectability and can be neglected in the measurements.

(iv) The last systematic error involved in the data comes from the uncertainties in contact line position. We assign a ± 2-pixel error bar (determined by the width of the transition area between the brightest and the darkest regions on the image) to both the x- and y-positions of the contact line. We look for the most likely contact line location by using mass conservation. Since there should be no mass sinks or sources in the experiment, the net flow through a closed surface should be zero. For simplification, we choose the closed surface formed by the tube surface, the liquid/air surface, and a circular arc with its centre at the contact line. With error-free velocity measurements, only the correct contact line position gives zero experimental net flow through this closed surface. Thus, we find the most likely experimental contact line position by minimizing the total flow through the closed surface among all the possible contact line positions. The departure from zero of the minimized net flow comes from the uncertainties in the velocities. Taking the cylindrical geometry effect (see §3.2) into account, the final result indicates that all contact line positions within the 5×5 box are statistically indistinguishable and must be considered valid.

The uncertainty in the contact line position moves the interface shape data slightly, causing statistically insignificant changes in the fitting parameter, $\omega_0 (\leqslant 0.01^\circ)$ and in χ^2 for the fit of the interface data (Chen *et al.* 1995). It does not change the x- and y-components of the measured velocity. However, the contact line position changes the spatial position relative to the contact line assigned to each velocity datum. To probe the effect of the contact line uncertainty on the velocity field, we subtract the same data set for two different, but possible, contact line positions. The subtraction is the difference of the velocity at the same spatial position relative to the contact line, using linear interpolations to provide data points at the same (r, ϕ) position. At $Ca = 0.10$, the differences are less than ± 0.01 in magnitude and $\pm 0.5^\circ$ in direction. At $Ca = 0.43$, the corresponding uncertainties are ± 0.002 and 0.2°. The impact of the contact line uncertainties correlates with the velocity gradient. Because the velocity gradients are large near the contact line, the contact line uncertainties have more

Ca	Component	$-200 < r < 0$ μm	$0 < r < 200$ μm	$r > 200$ μm
0.10	Magnitude	± 0.04	± 0.01	± 0.005
	Direction	$\pm 3°$	$\pm 3°$	$\leqslant 1.50°$
0.43	Magnitude	± 0.02	± 0.01	± 0.005
	Direction	$\pm 2°$	$\pm 2°$	$\leqslant 1.50°$

TABLE 1. Uncertainties in theoretical velocities due to contact line positions

impact on the velocity near the contact line than far away. Likewise, because the velocity gradients at comparable distance from the contact line are smaller at higher *Ca*, the velocity error due to the contact line uncertainty is smaller at $Ca = 0.43$ than at $Ca = 0.10$.

Finally, we determine the experimental reproducibility of the data by subtracting data sets taken from different runs but identical *Ca*. As shown in figure 4, the data sets at $Ca = 0.43$ show a systematic difference of less than 0.002 in the magnitude and 0.2° in the direction. This reproducibility is consistent with the potential systematic errors described above and is dominated by the uncertainties in the contact line position. The reproducibility at other *Ca* is similar to that at $Ca = 0.43$.

2.3. *Uncertainties in theoretical velocities*

In this subsection, we discuss the random and systematic uncertainties in the velocities predicted by (1) and (2). These uncertainties arise from the uncertainties in the experimentally measured spatial position and interface angles which are inputs used to evaluate the velocity.

The random uncertainty in the theoretical velocities arises from the standard deviation of the input interface angle, $\beta(r)$, of about 0.5° due to random pixel noise. This random uncertainty propagates through the modulated-wedge solution and produces an uncertainty of ± 0.002 in the magnitude and $\pm 0.5°$ in the direction of the predicted velocity.

There are two sources of systematic uncertainty. (i) Uncertainties in the contact line position change the input interface angles. Thus, each choice of contact line position leads to a systematically different theoretical velocity field. (ii) When particles move outside of the focal plane, the apparent particle position is shifted in the negative x-direction relative to the real particle position. Each of the uncertainties is discussed below.

(i) The input interface angle β for the theory is determined as

$$\beta_i = \arctan\left(\frac{y_i - y_{cl}}{x_i - x_{cl}}\right) + \pi/2, \tag{5}$$

where (x_i, y_i) is the position of the interface and (x_{cl}, y_{cl}) is the position of the contact line. The uncertainties in the contact line position, ± 2 pixels, move β_i systematically. This effect is not uniform in r. The interface shape difference for two possible contact line positions stays below 0.5° for $r > 200$ μm and increases rapidly to 1° at $Ca = 0.10$ and to 3° at $Ca = 0.43$ as r gets smaller. These uncertainties in the β_i lead to the theoretical velocity uncertainties (see table 1). Statistically significant uncertainties appear at $-200 < r < 0$ μm for the velocity magnitude and $-200 < r < 200$ μm for the velocity direction.

(ii) Since some particles move in planes which are not parallel to the focal plane (see

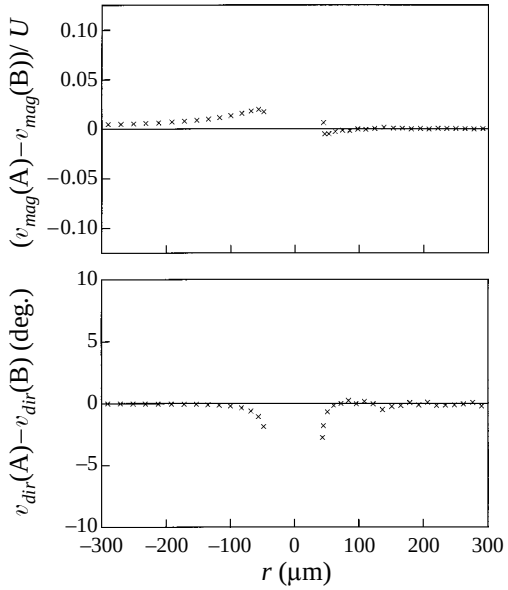

FIGURE 6. Typical error in theoretical velocity caused by particles outside the focal plane, $Ca = 0.10$. v_{mag} = magnitude of velocity. v_{dir} = direction of velocity. Labels A and B refer to positions A and B in figure 5.

figure 5), the positions of these particles appear closer to the contact line than they actually are. Although this position offset does not affect the measured particle velocity within our detectability (see §2.2), it causes systematic changes in the theoretical velocity, especially near the contact line where the velocity gradient is the highest and a small shift in position causes a large change in the theoretical velocity. The position offset is in the negative x-direction and we estimate that it is smaller than 1.5 μm in most of the experiments. The magnitude of the calculated velocity thus is systematically higher by ~ 0.02 than the correctly predicted velocity at small $r < 0$; and the direction is systematically off by $\sim -2°$ at small r (both $r < 0$ and $r > 0$) (see figure 6 for example), where the velocity gradient is the highest. This systematic error is smaller at higher Ca since the velocity gradient sampled by observable particles is smaller.

We have direct experimental evidence of this systematic error in theoretical velocities. We track two particles following the same apparent fluid trajectory at different times in one experiment. Since the particles follow the same apparent trajectories, they should show the same deviation from the model. One particle has a slightly fuzzy image, indicating that it did not travel in the focal plane. It shows deviations (the data minus the theoretical velocity evaluated at the apparent particle position) that are compatible with the particle offset error shown in figure 6. The other particle has a sharp image, indicating that it travelled in the focal plane. It shows no deviation all the way to the closest distance to the contact line.

The largest errors due to particle position offset appear at negative small r and low Ca. This error can be detected more readily than other errors since it shows a negative deviation in the magnitude and positive in the direction for small r along a single trajectory. Since most of the particles are not precisely in the focal plane, most data points in the deviation plots at small r are contaminated to some extent by this error. Some particles show a larger effect. We have kept all the data points and will note those trajectories with the largest position errors in the deviation plots.

	Causes	*Ca*	Component	$-200 < r < 0$ μm	$0 < r < 200$ μm
Measured velocity	Contact line position	0.10	Magnitude	± 0.01	± 0.01
			Direction	$\pm 0.5°$	$\pm 0.5°$
		0.43	Magnitude	Not significant	Not significant
			Direction		
Predicted velocity	Contact line position	0.10	Magnitude	± 0.04	± 0.01
			Direction	$\pm 3°$	$\pm 3°$
		0.43	Magnitude	± 0.02	± 0.01
			Direction	$\pm 2°$	$\pm 2°$
	Motion outside focal plane	0.10	Magnitude	-0.02	Not significant
			Direction	$+2°$	$+2°$
		0.43	Magnitude	Not significant	Not significant
			Direction		

TABLE 2. Statistically significant systematic errors

Table 2 summarizes all statistically significant systematic errors, i.e. those equal to or larger than the random error (0.01 in magnitude and 1.5° in direction). The information in table 2 enables us to compare two data sets, or a data set and its corresponding theoretical velocity field. Two data sets are statistically the same if their systematic difference is smaller than 0.01 in the magnitude and 1.5° in the direction. As we compare one data set and its corresponding theoretical velocity field, at small r, we allow ± 0.04 and $\pm 3°$ for $Ca = 0.10$, ± 0.02 and $\pm 2°$ for $Ca = 0.43$, due to the uncertainties of the contact line positions. We also allow -0.02 and $+2°$ at small r for $Ca = 0.10$, due to particles travelling outside the focal plane. Note that, while the contact line effect is fully random with respect to all possible contact line positions, the particle position offset causes systematic deviation at small r and small Ca and the effect has unique sign.

3. Results and discussion

3.1. *General characteristic of the velocity field*

The measured velocity fields confirm the qualitative features of previous studies. Figure 3 illustrates the characteristic rolling type of motion near the moving contact line. This agrees with the qualitative measurements made by Dussan & Davis (1974) using food dye. Figure 7 shows that the velocity component tangential to the solid surface approaches the solid velocity at several locations on the solid surface at $Ca = 0.43$. These results show that the no-slip boundary condition holds at least as close as ~ 100 μm from the moving contact line. Thus, the no-slip assumption of the classical hydrodynamic model holds at 100 μm for $Ca = 0.43$. The data point taken at 2 cm below the contact line demonstrates the no-slip condition without extrapolation and verifies our experimental technique.

3.2. *Comparison between data and theoretical velocity field*

To test the modulated-wedge solution, we compare the measured and predicted flow fields. We evaluate the theoretical velocity at the same spatial position as the experimental data point. In addition to the spatial position, the input to the theory also includes the measured interface polar angle $\beta(r)$. To identify systematic deviations of the data from the theory, we plot the differences of the data from the theory against the distance from the contact line, r.

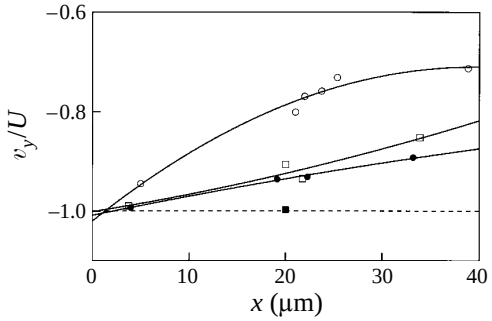

FIGURE 7. Scaled v_y versus x at different heights y from the contact line. Circles, $y = -100$ μm (intercept of 2nd-order polynomial fit: -1.020 ± 0.026); squares, $y = -200$ μm (intercept: -1.001 ± 0.004); solid circles $y = -300$ μm (intercept: -1.008 ± 0.004); solid square, $y = -2$ cm (1 data point at -0.9976).

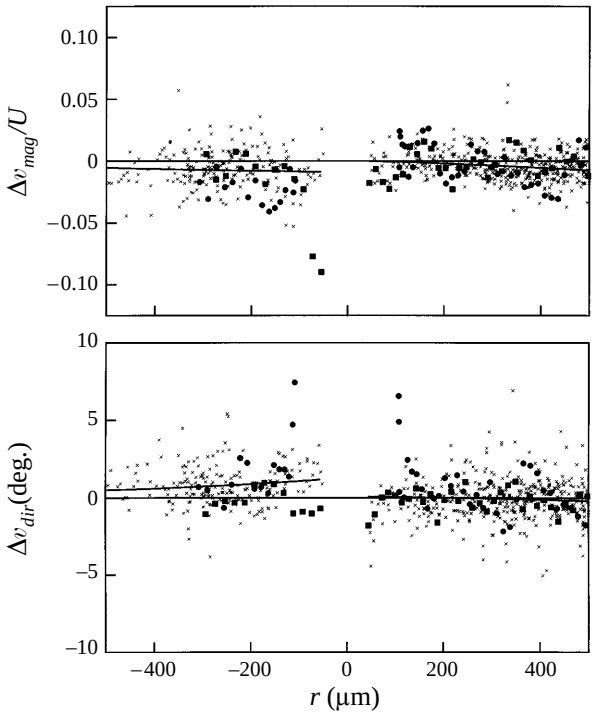

FIGURE 8. Deviation plots at $Ca = 0.10$ for 1 in. diameter tube. Solid circles and squares are two particles possibly out of focal plane.

Before discussing our results, we address the discrepancy in the flow field due to the fact that our experimental geometry is axially symmetric and the geometry assumed in the modulated-wedge model is planar. While a flat plate is the ideal solid to mimic this planar geometry, optical difficulties associated with using a flat plate (e.g. focusing on a two-dimensional liquid/air interface, finding the correct contact line position) lead us to use a large-radius cylinder. As a result, the two-dimensional wedge flow of the model is a good approximation to the experimental flow only for sufficiently small distances from the contact line.

The velocity fields in the planar and axially symmetric geometries differ because the effective area moving away from the solid increases in the cylindrical geometry but

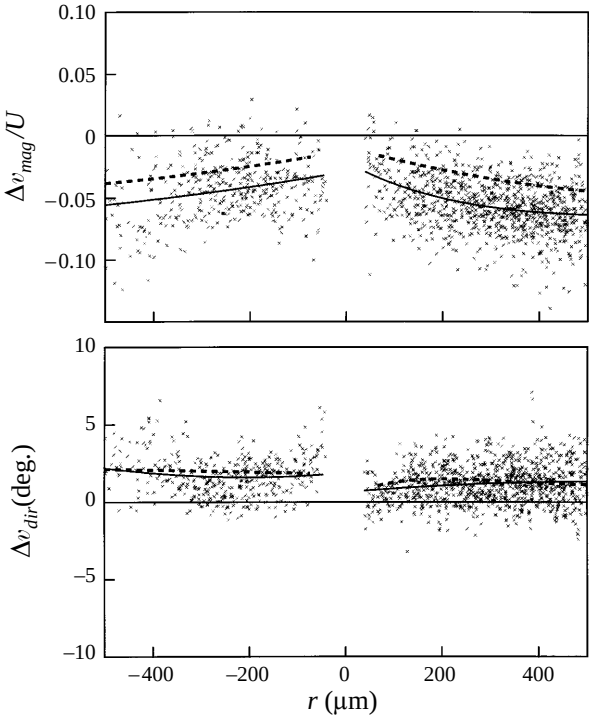

FIGURE 9. Deviation plots at $Ca = 0.43$. Data for 1 in. diameter tube. Solid line: 2nd-order polynomial fit to data from 1 in. diameter tube. Dashed line: 2nd-order polynomial fit to data from 2 in. diameter tube.

stays constant in the two-dimensional planar geometry. By mass conservation, for the same solid velocity, the fluid velocity in the cylindrical geometry is lower than in the planar geometry. Thus, the axial symmetry in our experimental geometry introduces an artifact as we test the validity of the modulated-wedge solution. To estimate this effect, we compare the velocities measured with a 1 in. diameter tube and a 2 in. diameter tube. At $Ca = 0.10$, the difference is less than 0.01 in the magnitude and 1° in the direction. This is similar to the uncertainties in the data for $-400 < r < 500$ μm. At $Ca = 0.43$, the difference is not negligible, 0.02 in magnitude and 1° in the direction, and is discussed below.

We can now compare our measurements with the modulated-wedge solution. We plot the difference between the data and the theory at $Ca = 0.10$ in figure 8. The deviation in the first 500 μm is within 0.01 for the velocity magnitude, and 1.5° for the direction. As discussed above, the discrepancy introduced by the cylindrical geometry is negligible in this region. Thus, at $Ca = 0.10$, the modulated-wedge solution describes the flow in this region within our detection levels.

Deviation plots at $Ca = 0.43$ are shown in figure 9 for a 1 in. diameter tube. As shown, the velocity data for the 1 in. and 2 in. diameter tubes differ. Thus, the deviation from theory for the 1 in. diameter tube must be at least partially due to the cylindrical geometry effect. For the 2 in. diameter tube, the data still deviate from the modulated-wedge solution all the way to our inner detectability limit (e.g. -0.02 in magnitude at $r \sim 30$ μm). This deviation is greater than our uncertainties and is independent of the contact line position. Thus, the deviations are due to the cylindrical geometry or to a breakdown of the modulated-wedge solution. For the 2 in. diameter

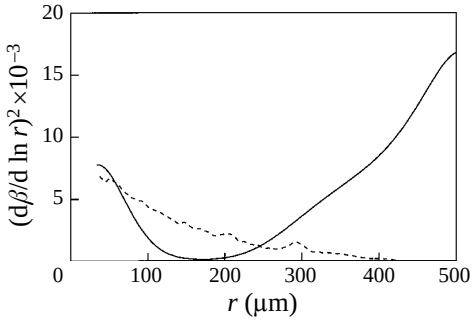

FIGURE 10. The square of the dimensionless interface curvature at $Ca = 0.10$ (dashed line) and 0.43 (solid line).

tube, at $r \sim 30$ μm, the distance from the solid surface is as small as 1/850 of the tube radius. Therefore, the cylindrical geometry effect is not likely to be significant and the observed deviation at $r \sim 30$ μm and $Ca = 0.43$ probably arises from the breakdown of the modulated-wedge solution. The deviations from the theoretical flow field at other Ca tested (0.07, 0.15, 0.20, 0.28) show the same trend as at $Ca = 0.10$ and 0.43, i.e. as Ca increases, the deviation increases.

As noted in §1, for the modulated-wedge solution to accurately describe the flow, $(d\beta/d\ln r)^2$ should be $\ll 1$ in a region much smaller than the container dimensions. The container dimension is ~ 5 cm (a 10 cm × 10 cm container with the tube at the centre), which is more than 50 times larger than the observed region near the contact line. To test for any effects of the container size, we compare the measured interface shapes and the flow fields with the tube at 5 cm and 2 cm from the container wall at $Ca = 0.43$. We find no detectable difference for the two measurements, indicating that macroscopic flows on the container length scale play no detectable role in the region we examine. Thus, flows at the container length scale do not produce the observed deviations from the theory. To test the condition $(d\beta/d\ln r)^2 \ll 1$, we measure $(d\beta/d\ln r)^2$ at $Ca = 0.10$ and $Ca = 0.43$ versus r from our interface shape data. As we see in figure 10, the local values of $(d\beta/d\ln r)^2$ at ~ 30 μm are on the same order (~ 0.007) for $Ca = 0.10$ and $Ca = 0.43$. Since the theory successfully describes the data at $Ca \leqslant 0.10$ and $r < 500$ μm, the breakdown of the theory at $Ca = 0.43$ and small r is not caused by the local $(d\beta/d\ln r)^2$. As r increases, $(d\beta/d\ln r)^2$ at $Ca = 0.43$ gets much larger than that at $Ca = 0.10$. At ~ 2500 μm, we find a maximum $(d\beta/d\ln r)^2 \sim 0.015$ for $Ca = 0.10$ and at least ~ 0.081 for $Ca = 0.43$. Thus, the breakdown of the theory at $Ca = 0.43$ may be the result of the higher $(d\beta/d\ln r)^2$ at larger r. This non-locality of the high-$(d\beta/d\ln r)^2$ breakdown is consistent with our discussion in §1.

Qualitatively, the interface shape and flow field results are compatible. The interface shape and modulated wedge solutions both hold in the first 400 μm at $Ca \leqslant 0.10$. Our previous study of the interface shape shows that the interface-shape theory overpredicts the interface curvature for $Ca > 0.10$. In the modulated-wedge theory, the normal stress, which sets the interface curvature, comes mostly from the fluid pressure contribution as opposed to velocity gradient contribution, $Ca\,\boldsymbol{n}\cdot(\boldsymbol{\nabla} v + (\boldsymbol{\nabla} v)^T)\,\boldsymbol{n}$ (v is the fluid velocity and $\boldsymbol{n}$ is the unit outward normal of the interface). The higher interface curvature predicted by the interface-shape model requires a larger fluid pressure jump across the interface than the observed interface curvature. Therefore, taking the air pressure to be zero for convenience, the fluid pressure predicted by the theory in the intermediate region is more negative than the actual pressure. This more negative

theoretical pressure next to the surface creates a higher pressure gradient along the interface which drives the fluid toward the contact line faster than the observed velocity. Thus, the higher curvature predicted by the interface shape model leads to a higher fluid velocity toward the contact line. This agrees with the comparison of our measured flow field and the predictions of the modulated-wedge solution (see §3.2).

3.3. *Geometry freedom*

The geometry-independent interface shape and flow field in the intermediate region, where classical hydrodynamics hold, are the necessary boundary conditions for the prediction of the macroscopic spreading dynamics. The geometry-free information can act as the boundary condition at smaller distances from the contact line for numerical calculations of spreading fluids based on the Navier–Stokes equation and classical boundary conditions at the solid/liquid and liquid/air interfaces.

Macroscopic length scales and configurations affect the size of the geometry-free region. These macroscopic geometry-dependent factors are the tube radius, capillary length, container dimensions, and tube immersion angle. In a geometry-free region, the interface shape and flow field should be asymptotically insensitive to all these factors. In the model we employ here, the geometry-free region is the intermediate region (Cox 1986). This region is a wedge-like two-dimensional domain formed by a flat solid surface and a fluid/fluid interface. In this wedge-like region, the interface shape behaves as described by equation (1) in Marsh *et al.* (1993). The flow field is described by (1) and (2) (the modulated-wedge theory) as discussed in §1. Since the interface shape and flow field in this wedge-like region represent the limit of all Stokes flows approaching a moving contact line (Dussan & Davis 1974), the geometry-free information of the intermediate region enables one to transfer boundary conditions among different geometries for the same material system.

The geometry-free region should be simultaneously independent of all the macroscopic geometry factors and is only free from all macroscopic influence in an asymptotic sense. Experimentally, we can determine this region when the residual geometry dependence drops below the detection limits of our techniques. We define the size of the geometry-free region as that of the largest region where the interface shape and flow field are independent of all macroscopic factors.

In our experiment, we vary the immersion angle, tube radius, and container size. To find the geometry-free region at $Ca = 0.43$, we perform the following three steps.

(i) As discussed in §3.2, we change the position of the tube relative to the container wall (i.e. we change the container dimensions) while keeping the tube diameter at 1 in. and the immersion angle at 90°. As the distance of the tube from the container wall shortens from ~ 5 cm to ~ 2 cm, the interface shape and the flow field are indistinguishable (within our detectability limit) throughout the field of view (~ 1200 μm).

(ii) Using the 1 in. diameter tube, we change the immersion angle of the tube from 90° to 70° in a similar way to Chen *et al.* (1995). In that work, we showed that the interface shapes are indistinguishable in the first ~ 100 μm for the two immersion angles. Comparison of flow fields requires that the compared flow domains occupy the same physical space. Therefore, we can only compare flow fields from the tilted tube measurements in the region where the interface shapes overlap. In this region ($r \leqslant 100$ μm), the velocity fields are statistically the same for the two immersion angles (see figure 11) (we allow error bars of $0.01\sqrt{2}$ in magnitude and $0.5\sqrt{2}°$ in direction, based on error propagation for the difference of two quantities with error bars of 0.01 and 0.5°).

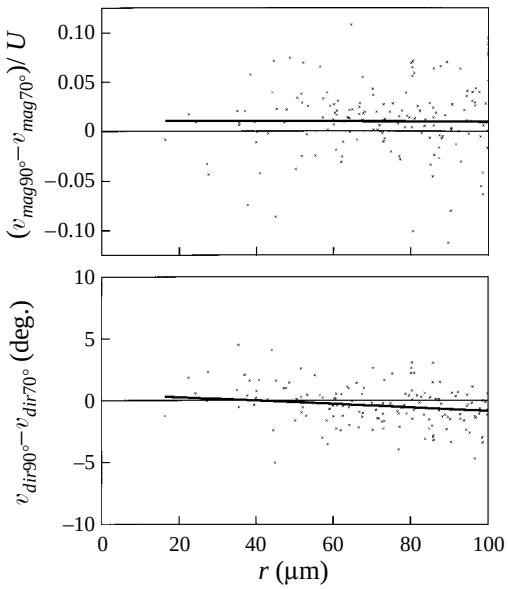

FIGURE 11. Flow field differences from the tilted tube experiments at $Ca = 0.43$.

(iii) As discussed in §3.2, when we change the tube diameter from 1 to 2 in., the interface shape stays the same whereas the flow field changes significantly. Thus, the impact of tube radius on the velocity field is stronger than on the local stress normal to the interface. Though the velocity data within ~ 100 μm of the contact line for a 1 in. tube are insensitive to the container size and immersion angle, the flow field still has a residual dependence on the tube radius (see figure 9). Even for the 2 in. tube, the flow field may still be contaminated by geometry dependence due to the tube size.

This study demonstrates the experimental techniques needed to find the geometry-free region. At higher Ca where the analytic solutions fail, the experimentally measured interface shape and flow field in the geometry-free region can provide the boundary condition for numerical solutions of the Navier–Stokes equation in the intermediate and outer regions where the classical boundary conditions may be applied at the solid/liquid and liquid/air interfaces.

4. Conclusions

In this work, we continue our study of asymptotic spreading models (Cox 1986; Dussan *et al.* 1991) through quantitative study of the flow field near the moving contact line. As PDMS spreads on a clean Pyrex surface, we make simultaneous measurements of the interface shape and flow field in the first few hundred microns from the contact line.

In our previous work, we showed that the model of the interface shape holds for $Ca \leqslant 0.10$ and $20 \leqslant r \leqslant 400$ μm. In this study, the measured two-dimensional flow field shows that the no-slip boundary condition on the solid/liquid interface holds at least as close as 100 μm to the contact line at $Ca = 0.43$. We compare the measured flow fields to the modulated-wedge solution of Cox (1986) at increasing Ca. We carefully incorporate experimental error analyses into the results and conclude that the model holds for $r < 500$ μm at $Ca = 0.10$. In the same region at $Ca = 0.43$, the model does not agree with our measurement, at least at our inner detectability limit (~ 30 μm from the contact line). The possible disagreement at $Ca = 0.43$ is due to the liquid/air interface

violating the assumption $(\mathrm{d}\beta/\mathrm{d}\ln r)^2 \ll 1$ of the model. The breakdown is a non-local effect, i.e. large $(\mathrm{d}\beta/\mathrm{d}\ln r)^2$ at large r can affect the performance of the modulated-wedge solution at small r. Since the modulated-wedge theory may break down at higher $(\mathrm{d}\beta/\mathrm{d}\ln r)^2$, care should be taken when using this theory to generate flow fields as boundary conditions for numerical calculations. However, all the velocity deviations we present here are $< 5\%$ of the spreading velocity. Depending on the accuracy requirement, the modulated-wedge theory may still be a good approximation at $Ca \sim 0.4$ near the moving contact line.

The results from our interface shape and flow field study are consistent. They both hold for $Ca = 0.10$ near the contact line, and both overpredict the normal stress in the vicinity of the moving contact line at higher Ca. The overpredicted normal stress is consistent with the well-known stress singularity which arises from classical hydrodynamics.

Beyond the analysis of the analytical models, the results of this study are the measurement and identification of geometry-free interface shapes and flow fields near the moving contact line. This geometry-free information constitutes the boundary condition transferable among different macroscopic geometries. Our experimental techniques provide a means for determining the geometry-free region. Since the size of this region in a new geometry need not coincide with that in the experimental measurement, one can use the theory for the interface shape and flow field together with the measurement to generate boundary conditions in the wedge-like region of the new geometry. In this process, the identification of the geometry-free boundary condition in the new geometry requires that the macroscopic results of the calculation in the new geometry be insensitive to the location where the boundary conditions are applied. This lack of the sensitivity is characteristic of the behaviour of the intermediate region described in the model (Cox 1986; Dussan *et al.* 1991).

We wish to acknowledge the support of NASA from grant no. NAG3-1390.

REFERENCES

Chen, Q., Ramé, E. & Garoff, S. 1995 The breakdown of asymptotic hydrodynamic models of liquid spreading at increasing capillary number. *Phys. Fluids* **7**, 2631.

Cox, R. G. 1986 The dynamics of the spreading of liquids on a solid surface. Part 1. Viscous flow. *J. Fluid Mech.* **168**, 169.

Dussan, V., E. B. 1976 The moving contact line: the slip boundary condition. *J. Fluid Mech.* **77**, 665.

Dussan, V., E. B. 1979 On the spreading of liquids in solid surfaces: static and dynamic contact lines. *Ann. Rev. Fluid Mech.* **11**, 371.

Dussan, V., E. B. & Davis, S. H. 1974 On the motion of a fluid-fluid interface along a solid surface. *J. Fluid Mech.* **65**, 71.

Dussan, V., E. B., Ramé, E. & Garoff, S. 1991 On identifying the appropriate boundary conditions at a moving contact line: an experimental investigation. *J. Fluid Mech.* **230**, 97.

Gennes, P. G. de 1985 Wetting: static and dynamics. *Rev. Mod. Phys.* **57**, 827.

Gennes, P. G. de, Hua, X. & Levinson, P. 1990 Dynamics of wetting: local contact angles. *J. Fluid Mech.* **212**, 55.

Hocking, L. M. 1977 A moving fluid interface. Part 2. The removal of the force singularity by a slip flow. *J. Fluid Mech.* **79**, 209.

Hocking, L. M. & Rivers, A. D. 1982 The spreading of a drop by capillary action. *J. Fluid Mech.* **121**, 425.

Huh, C. & Mason, S. G. 1977 The steady movement of a liquid meniscus in a capillary tube. *J. Fluid Mech.* **81**, 401.

Huh, C. & Scriven, L. E. 1971 Hydrodynamics model of steady movement of a solid/liquid/fluid contact line. *J. Colloid Interface Sci.* **35**, 85.

Inoue, S. 1986 *Video Microscopy*. Plenum.

Kistler, S. 1994 *Wettability*, Chapter 6. Marcel Dekker.

Marsh, J. A. 1992 Dynamic contact angles and hydrodynamics near a moving contact line. Doctoral thesis, Dept. of Physics, Carnegie Mellon University, Pittsburgh.

Marsh, J. A, Garoff, S. & Dussan, V., E. B. 1993 Dynamic contact angle and hydrodynamics near a moving contact angle. *Phys. Rev. Lett.* **70**, 2778.

Mertzkirch, W. 1974 *Flow Visualization*. Academic.

Moffatt, H. K. 1964 Viscous and resistive eddies near a sharp corner. *J. Fluid Mech.* **18**, 1.

Ngan, C. G. & Dussan, V., E. B. 1982 On the dynamics of liquid spreading on solid surfaces. *J. Fluid Mech.* **209**, 191.

Ramé, E. & Garoff, S. 1996 Microscopic and macroscopic dynamic interface shapes and the interpretation of dynamic contact angles. *J. Colloid Interface Sci.* **177**, 234–244.

Savitzky, A. & Golay, M. J. E. 1964 Smoothing and Differentiation of Data by Simplified Least Squares Procedure. *Anal. Chem.* **36**, 1627.

Thompson, P. A. & Robbins, M. O. 1990 Shear flow near solids: epitaxial order and flow boundary conditions. *Phys. Rev.* A **41**, 6830.

Tuck, E. O. & Schwartz, L. W. 1990 A numerical and asymptotic study of some third-order ordinary differential equations relevant to draining and coating flows. *SIAM Rev.* **32**, 453.

Voinov, O. V. 1994 Closure of the hydrodynamic theory of wetting in a small-scale region. *J. Appl. Mech. Tech. Phys.* (translated from Russian) **35**, 1.

Yang, J. X., Koplik, J. & Banavar, J. R. 1992 Terraced spreading of simple liquids on solid surfaces. *Phys. Rev.* A **46**, 7738.